Experiments in Fluids (2023) 64:37
https://doi.org/10.1007/s00348-023-03579-x

RESEARCH ARTICLE

Effect of environmental disturbances on crossflow instability

Marco Placidi[1] · Richard Ashworth[2] · Chris J. Atkin[3] · Stephen Rolston[2]

Received: 1 February 2022 / Revised: 16 November 2022 / Accepted: 5 January 2023 / Published online: 3 February 2023
© The Author(s) 2023

Abstract
Wind tunnel experiments on the receptivity of three-dimensional boundary layers were performed in a range of freestream turbulence intensities, *Tu*, from 0.01%—the lowest level ever achieved in this type of work—up to 0.41%. This work confirms that for $Tu = 0.01\%$, and presumably below this level, the transition process is dominated by stationary modes. These are receptive to surface roughness and generate Type-I and Type-II secondary instabilities that eventually cause the transition to turbulence. The saturation amplitude of these stationary waves is highly sensitive to the level of environmental disturbances; the former is here recorded to be the highest in the literature, with the latter being the lowest. Travelling modes are still present; however, their influence on the transition process is marginal. At matched surface roughness levels, when the level of environmental disturbance is enhanced to $Tu \geq 0.33\%$, the travelling modes acquire more importance, strongly influencing the laminar/turbulent transition process, whilst the initial amplitude and growth of the stationary modes are hindered. For this level of *Tu*, is the interaction of steady and unsteady disturbances that produces highly amplified waves (Type-III), that quickly lead to nonlinear growth and anticipated turbulence. Finally, a simple rule of thumb is proposed, where the transition front was found to move forward by roughly 10% chord for an increase in one order of magnitude in the *Tu* levels.

1 Introduction and background

Numerous numerical and experimental studies have investigated the role of external influences and initial conditions on the stability of three-dimensional boundary layers as those developing over aircraft's wings. Deyhle and Bippes (1996) considered the receptivity of the boundary layers to different surface roughness geometries and environmental conditions. By examining the effect of sound on the stability of three-dimensional boundary layers, they found that neither the disturbance growth nor the transition front location was affected by the increased sound levels, concluding that three-dimensional boundary layers are only very weakly receptive to sound, while this does largely contribute to the initial amplitude of Tollmien–Schlichting (T–S) waves. This topic is further explored in Placidi et al. (2020), hence omitted here together with most of the previous works that considered the role of environmental disturbances on the stability of two-dimensional flows, which is not relevant here. Deyhle and Bippes (1996) also conducted experiments in several facilities with freestream turbulence intensity in the range of $0.08\% \leq Tu \leq 0.57\%$, where *Tu* represents the ratio of the root-mean-squared (*rms*) of the velocity fluctuations to the freestream velocity U_∞. They observed that an increase in *Tu* produces larger initial travelling mode amplitudes, whilst reducing the growth rate of the stationary crossflow modes. They also concluded that for $Tu > 0.2\%$, travelling modes dominate the instability. As the flight environment is characterised by much lower FreeStream Turbulence (FST) (Saric 2008; Carpenter et al. 2009; Saric et al. 2011; Guissart et al. 2021), the stationary modes are considered more relevant for aircraft applications, and hence have typically received more attention in the literature. Bippes and Lerche (1997) also conducted work on crossflow instability and reported that, while the initial amplitude of the stationary mode is set by surface roughness, the initial amplitude of the travelling disturbances is set by the level of FST. Many of the findings of boundary layer receptivity drawn by the German group were confirmed in the USA, and a control strategy for crossflow instability by the mean of micron-sized Discreet Roughness

✉ Marco Placidi
m.placidi@surrey.ac.uk

[1] Department of Mechanical Engineering Sciences, University of Surrey, Guildford GU2 7X, UK

[2] Airbus Group Central Research and Technology, Airbus Wing Integration Centre, Building 07Y, Bristol BS34 7PA, UK

[3] Department of Engineering, University of East Anglia, Norwich NR4 7TJ, UK

Elements (DREs) was developed (Hunt 2011; Reibert 1996; Carrillo et al. 1996; Saric et al. 2011; White and Saric 2005; Carpenter et al. 2010; Dagenhart and Saric 1999; Saric et al. 1998a; Radeztsky et al. 1999). Excitation of 3-D instabilities via DREs has, from then, been the most commonly used, however, we do highlight other options—see, e.g. Borodulin et al. (2018), Paula et al. (2017), Yadala et al. (2018), van Bokhorst (2018), Bertolotti (2000), Baranov et al. (2021), Katasonov and Sadovskiy (2021), and Sharma and Sengupta (2019). White et al. (2001) further confirmed that, for $Tu = 0.04\%$, the transition is dominated by the stationary modes, but when the Tu level is enhanced by a turbulence grid to 0.25%, travelling modes were responsible for the transition to turbulence. Travelling disturbances were also identified in low-turbulence environments; however, their amplitude was typically an order of magnitude smaller than that of the stationary modes (Dagenhart and Saric 1999). Preliminary experiments by Hunt (2011) found a small reduction in the initial stationary disturbance amplitude for increasing levels of FST (from $Tu = 0.02\%$ to 0.035%). Travelling modes of significant amplitude have also been observed by Eppink (2014) at $Tu = 0.02\%$; however, the focus of this study was on surface discontinuities. The work in Downs (2012) and Downs and White (2013) is one of the rare examples for which a range of FST ($Tu < 0.2\%$) is systematically considered. They observed that environmental disturbances contribute to the excitation and growth of unsteady disturbances, while also affecting the growth of stationary crossflow modes. Further evidence also suggests that for a fixed level of FST, the importance of travelling crossflow instabilities increases with a reduction in the roughness level (Takagi and Itoh 1994). Kurian et al. (2011) and Borodulin et al. (2013) confirmed the linear character of the boundary layer receptivity to FST for the range of turbulence levels and length scales considered. They also further confirmed that for increasing Tu, travelling modes start to dominate the transition, inhibiting the growth of the stationary disturbances. Borodulin et al. (2019) successfully validated measured stability characteristics of unsteady crossflow modes with various theoretical approaches. Fransson et al. (2005) not only suggested a reliable way to calculate the intermittency factor, and hence the transition front locations, but also showed how this information can be encapsulated in transition prediction models. Chernyshev et al. (2011) compared the effect of FST on the stability of 2-D laminar aerofoil with that of a swept-wing model showing that, for both cases, higher FST reduced the transition N-factors.

The synergy of numerical simulations and experimental work (Groot et al. 2018) have greatly contributed to our understanding of the physics of the problem. Schrader et al. (2009) shed light on the interactions between surface roughness and FST in swept-flat-plate boundary layers. They used a vortical disturbance superposed on the mean flow and found that, although the vortical mode alone does excite travelling mode growth, it is its interaction with the steady disturbances that produces highly amplified waves; i.e. the travelling modes are a result of coupled roughness and turbulence receptivity, as further confirmed in Downs and White (2013). Haynes and Reed (2000) demonstrated that these interactions reduce the growth rate of the stationary modes, leading to nonlinear saturation. Schrader et al. (2010b) confirmed that the FST excites unsteady crossflow modes resulting from a linear receptivity mechanism, while the subsequent growth of the primary modes rapidly becomes nonlinear leading to saturation for high FST. They also confirmed that the initial amplitude of the perturbations scales linearly with the level of Tu, nevertheless, larger turbulence intensities amplify the effect of the nonlinearities. Schrader et al. (2010a) indicated that when FST and small surface roughness (of the height of one-tenth of the local displacement thickness) are employed in combination, the transition process is dominated by steady disturbances until the Tu remains below 0.5%. Fransson and Shahinfar (2020) showed that the transition location is advanced by increasing the turbulence intensity, however, the integral length scale of the turbulence, Λ, has an opposite effect on the transition onset at low and high Tu. In the former, the transition is postponed by decreasing Λ, while the opposite is true in the latter (i.e. high Tu). Crouch et al. (2015), to the best of our knowledge, offers the most recent comprehensive study of the effect of Tu on crossflow instability. Their summary confirms that for low-turbulence environments ($Tu << 0.2\%$) the transition is dominated by roughness-induced stationary crossflow. For high-turbulence levels ($Tu > 0.2\%$) and relatively smooth surfaces instead, the transition process is dominated by unsteady disturbances. Finally, both surface roughness and FST influence the receptivity for conditions at moderate levels of environmental disturbances. Extended summaries of some of these topics, and beyond, are contained in Nitschke-Kowsky and Bippes (1988), Saric et al. (2002), Butler and Wu (2018), Saric et al. (2003).

As a result of these studies and the theoretical framework underpinning Linear Stability Analysis (LSA) much more is known regarding the amplification of unstable waves in three-dimensional flows, however, the development of a genuine transition prediction tool is limited by the necessity to model the 'receptivity' (Morkovin 1969) of the boundary layers to external disturbances. Unfortunately, most of the experimental work on this problem has been performed in different facilities, while numerically, the lack of a unified theory to model receptivity (or the omission of this process altogether) has rendered the comparison across different datasets rather challenging (Reed and Saric 1989), hindering a thorough physical understanding of the receptivity (Downs and White 2013). This work, therefore, further

explores the sensitivity of stationary and travelling modes to FST, by providing additional data relevant to the flight environment where the Tu is extremely low. These conditions were achieved by exploiting the uniquely low FST of our facility ($Tu = 0.01\%$) and by enhancing it via the means of two turbulence screens, which produced $Tu = 0.33\%$ and $Tu = 0.41\%$, respectively. By doing so, we can increase the FST level by one order of magnitude within the linear limit $Tu < 5.06\%$ (Schrader et al. 2010b), whilst keeping the roughness conditions fixed via the means of DREs of fixed height. Except for the adoption of the DREs, here, we consider the natural transition process where no active forcing is applied; this is in contrast with some of the previous work (van Bokhorst and Atkin 2017; Serpieri and Kotsonis 2018). The integral length scale of the turbulence is also roughly constant across all the cases considered. These experiments are designed to provide data on the switching between stationary- and travelling- crossflow-dominated instabilities to facilitate future numerical modelling. The aim is to correlate the increase in Tu with the movement of the transition front, which encompasses the cumulative effect of FST and surface roughness receptivity on crossflow modes.

2 Experimental facility, setup and details

2.1 Experimental facility

Experiments were conducted in the closed-circuit Gaster low-turbulence wind tunnel at City, University of London. The turbulence intensity, measured in the empty tunnel, was less than 0.006% of the freestream velocity, U_∞, within the frequency range 4 Hz–4 kHz at $U_\infty = 16$ m/s, which was the speed used in this work. The temperature in the laboratory environment, where tunnel air bleeds, is computer controlled and stable throughout the day and night. Typically, this results in experimental runs where the temperature variation is below 1 °C; the effect of this temperature change is compensated by the calibration procedure, as highlighted in Sect. 2.7. Based on the conditions within the tunnel test section, the air kinematic viscosity varied in the range $\nu = 1.4902 \times 10^{-5} \pm 0.47\%$ m^2 s^{-1}, with the Reynolds number based on the plate chord in the range $1.65 \times 10^6 < \mathrm{Re}_c < 1.66 \times 10^6$. The tunnel test section measures $3 \times 3 \times 6$ ft^3, and is equipped with a 3-axis traverse system with a resolution and reliability of ± 0.1 mm in the x- and z-axes, whilst the wall-normal y-axis is accurate to ± 0.005 mm. The origin and directions of the coordinate system adopted herein are indicated in Fig. 1. The former is considered to be in the centreline of the tunnel test section

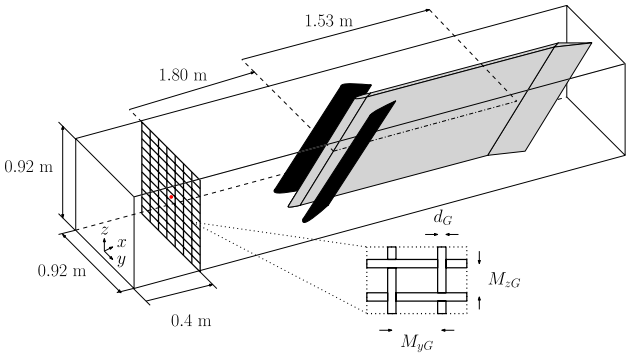

Fig. 1 Schematic of the wind tunnel setup and turbulence screens. Displacement bodies are visible in black, while the flat plate is identifiable in grey. The red dot identifies the origin of the coordinate system, whose principal directions are included at the bottom of the picture for visibility reasons

(both in y and z) and at the x location of the turbulence grid (as highlighted in Fig. 1).

2.2 Experimental setup

A combination of a nominally 45° swept flat plate and equally swept displacement bodies were used to create favourable conditions for the development of crossflow vortices, as shown in Fig. 1. The pressure gradient generated by the displacement bodies is further discussed in Sect. 2.4. The plate is made of 9.54 mm thick aluminium, and it measures 1535 mm in chord and 914 mm in span. Further details on this experimental setup are reported in van Bokhorst (2018). To excite the fundamental waves, circular DREs of 24 μm in height and 3 mm in diameter were positioned close to the neutral stability point and critically spaced laterally at the appropriate fundamental wavelength of the primary crossflow modes ($\lambda = 11.5$ mm). The height of the DREs, although seemingly small, is some orders of magnitudes larger than the background roughness of the model (rms < 0.25 µm measured with a Mitutoyo SJ-500 pathometer).

2.3 Turbulence enhancement

To systematically investigate the effect of FST on the development of crossflow instability at fixed roughness conditions, a range of Tu was examined. Two different turbulence grids (Grid I and Grid II in Table 1) were employed to increase the level of FST in the wind tunnel. Westin et al. (1994) showed that when a turbulence grid is installed upstream of the contraction, the resulting FST in the test section can be highly anisotropic. To avoid this problem, screens are installed downstream of the contraction, but upstream of the entrance to the test section, in a straight

section of the tunnel, which was purposely designed to introduce flow manipulation ahead of the models. The screens are 1.8 m upstream of the model leading edge, which corresponds to approximately 138 and 277 mesh widths (for Grid I and II, respectively). A certain distance downstream of the turbulence grid is required for the individual vortices generated by the grid elements to merge into homogeneous turbulence. This minimum distance is of the order of 20 times the mesh width (Fransson and Shahinfar 2020), which in this case is approximately 130 mm for Grid I and 260 mm for Grid II. The location of the screens should, therefore, guarantee that the model experiences nearly homogeneous incoming turbulence. This is further discussed in Sect. 3—see Figs. 4 and 5. The turbulence grids are characterised by the following parameters: freestream turbulence, integral length scale, and porosity/solidity. The freestream turbulence is defined in Sect. 1. The streamwise integral length scale is defined as $\Lambda_x = U_\infty \int_0^\infty R_{uu}(\tau)\,\mathrm{d}\tau$, where R_{uu} is the auto-correlation function of the velocity signal, and τ is its time lag (Fransson et al. 2005). Geometrically, a grid is characterised by its porosity, β, which is defined as the ratio between the open to the total area of the grid and can, therefore, be calculated as $\beta = \left(1 - \frac{d_G}{M_G}\right)^2$, where d_G and M_G are the bar diameter and mesh width, respectively (see Fig. 1). Finally, the grid solidity, σ, customarily reported in the literature, can be simply derived as $\sigma = 1 - \beta$.

2.4 Pressure coefficient

The pressure coefficient, C_p, imposed on the plate by the displacement bodies, is measured simultaneously via two distinct methods: static pressure ports embedded in the model surface and through a pressure belt wrapped around the whole length of the plate to better resolve the leading edge region, which is important for the analysis in Sect. 2.5. The pressure belt is made of thirty silicone pipes mounted side by side to each other for a final width of approximately 65 mm; each is equipped with a static port at a variable chordwise location. Figure 2 shows a comparison of the pressure coefficient acquired with the two different methodologies. Here, we refer to a $C_{\mathrm{p,3D}}$ defined using the freestream velocity normal to the leading edge, as for the analysis in Sect. 2.5. Despite the lack of embedded ports for $x/c < 0.1$ (due to the mechanical complications introduced by the interchangeable leading edge of the plate), the two datasets compare fairly well in the remaining chordwise range. Small discrepancies between the two data sets are believed to be due to (1) the local slight change in geometry due to the presence of the belt, (2) the measurement uncertainty, and (3) the unavoidable three-dimensionality in the pressure coefficient as the belt and the embedded ports are located at different spanwise

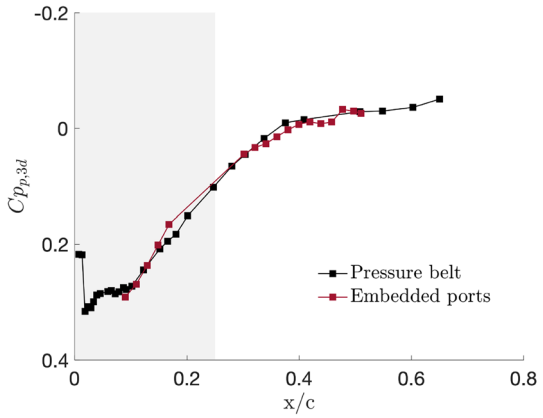

Fig. 2 Pressure coefficient along the streamwise direction of the flat plate. The grey shaded area indicates the location of the displacement body

locations across the plate. 3D effects, however, were found to be negligible within the measurement region, where, the C_p can be considered quasi-2D, as confirmed by numerical analysis [see van Bokhorst (2018) for further details]. Unsurprisingly, the initial amplitude of the disturbances was found to be strongly dependent on the pressure gradient induced on the flat plate; i.e. the displacement bodies setup and the trailing edge flap angle on the plate. These modify the circulation around the model, the location of the stagnation point, and ultimately the development of the disturbances. The data presented herein is obtained in one tunnel entry and strictly with the same setup. In particular, the DREs, the flaps angle and the pressure gradient were kept unchanged. The experimental data are too coarse to evaluate a reasonable evolution for the Hartree parameter, however, following the definition in Borodulin et al. (2013), this was found to be in the range $0 < \beta_\mathrm{H} < 0.4$.

2.5 Linear stability analysis

Linear stability analysis (LSA) was carried out both in the design phase of the experiment setup (the reader is referred to van Bokhorst (2018) for further details) and subsequently to inform and enrich the results of the experiments. A very brief overview of the numerical setup follows. The pressure distribution measured experimentally, together with the relevant flow conditions and geometrical setup are inputted in BL2D (Atkin 2004) a compressible laminar boundary layer code to provide a suitable base flow. The latter is then employed by CoDS (Atkin and Poll 1996) to solve a three-dimensional linear stability problem. The results of this procedure in terms of N-factor curves for the most relevant disturbances discussed herein are summarised in Fig. 3. Data are extracted from figures 9 and 34 in van

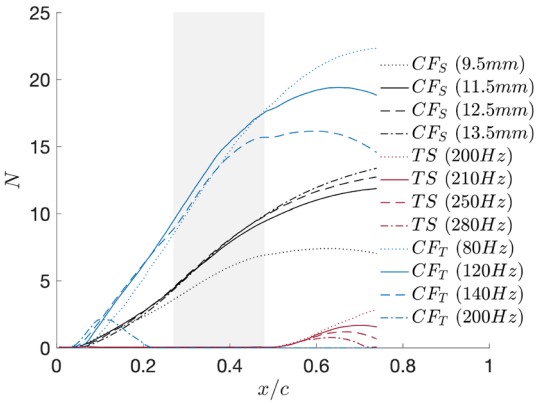

Fig. 3 *N*-factor curves obtained from linear stability analysis with the measured experimental pressure distribution in Fig. 2. The grey shaded area indicates the location of the hot-wire measurements. The data are taken from van Bokhorst (2018)

Bokhorst (2018). It is clear to see how both stationary and travelling modes are strongly amplified in the measurement region. The dominance of stationary crossflow disturbances with a spanwise wavelength of 11.5 mm in the low *Tu* case is achieved by the fundamental spanwise spacing of the DREs, as discussed in Sect. 2.2. Travelling disturbances are reported for the frequencies of interest (80 Hz $\leq f \leq$ 200 Hz), and similarly T–S waves in the range 200 Hz $\leq f \leq$ 280 Hz. These frequencies will be discussed in detail in Sect. 3.4 and Sect. 3.5, respectively.

2.6 Linearised Navies–Stokes methodology

The numerical modelling of surface roughness and receptivity to stationary crossflow via a Linearised Navier–Stokes (LNS) solver was conducted by Airbus Group Central Research and Technology. The growth of particular crossflow modes and their interaction with other modes was modelled by solving the linear parabolised stability equations using the methodology in Mughal (2006). Whilst this approach can capture the growth and interaction of modes it is not able to model the initial receptivity phase of the disturbance generation. For the latter, use was made of the solver described in Mughal and Ashworth (2013). Briefly, linearised Navier–Stokes equations are solved for a spanwise homogenous base flow and a given spanwise periodicity in the disturbance field; this is imposed in the experiments by DREs, as described in Sect. 2.2. Fourier decomposition of the span-periodic disturbance, results in a decoupled linear problem for each Fourier mode. A weakly nonlinear version of the code can solve simultaneously for a number of modes and their interactions; this was, however, not employed here. The results from the numerics are only used herein to validate the base flow in Sect. 3.1.

2.7 Instrumentation and hot-wire details

Time-resolved velocity measurements are obtained via a Dantec Constant Temperature Anemometry (M-unit), with a single miniature boundary layer hot-wire sensor (with effective sensing length $l \approx 1$ mm and diameter $d \approx 2.5\,\mu$m). The volts to velocity conversion is obtained via King's law fit, as highlighted in Bruun (1995). To minimise the calibration error, the probes are pre- and post-calibrated in situ in the velocity range 0.5 m/s $\leq U \leq$ 20 m/s against a Pitot-static tube connected to a Furness (FCO560) manometer. The latter has a resolution of 0.025% of its full-scale range, herein $\pm$15 Pa. Temperature correction is applied to the data, as in Bruun (1995), and the pre- and post- calibrations are used with appropriate weighting when processing the hot-wire data. Mean streamwise velocity and root-mean-squared (rms) of the bandpass-filtered velocity are denoted by capital letters and a prime, respectively. The hot-wire sensor is aligned normal to the line of flight (i.e. x direction) and, therefore, it is technically set to measure a Euclidean sum of the U and V velocities, $|\mathbf{V}| = \sqrt{U^2 + V^2}$. However, under the assumption that, $V^2 << U^2$, hereafter it is assumed that $|\mathbf{V}| = U$. Signals are acquired and digitised using a combination of National Instruments (NI) PXI6143 card and DAQ-BNC2021 module, coordinated via a NI PXI Chassis (NI PXI 1033) controlled via in-house LabView routines. The sampling frequency was kept fixed at 20 kHz throughout the tests and low- and high-pass filters were applied at 10 kHz and 2 Hz, via a PDS Instruments Ltd. Model 3362. Signals were acquired for 120 s, so each measurement point comprises 2.4×10^5 number of samples. The typical spatial resolution of the hot-wire scans is such that each crossflow vortex (over a spanwise wavelength of 11.5 mm) is resolved with nominally 1200 data points; these include over 50 points in the wall-normal direction (across a boundary layer depth that is below 8 mm at the furthest streamwise station), and 24 points in the spanwise direction. The hot-wire scans used to identify the transition front locations in Sect. 3.6 have a resolution of 0.5 mm so that the front location can be localised with an accuracy of $\pm 0.16\%c$. Spectra are obtained by Fast Fourier Transform algorithm (with a Hanning window) and a resolution of 2 Hz. The mean freestream velocity was set to 16 ms^{-1} with uncertainty, determined following Hutchins et al. (2009), below 2%.

2.8 Characterisation of the disturbance environment

As the selection of turbulence grid for FST enhancement purposes is largely an empirical process (Downs and White 2013), preliminary tests were performed on grids formed by solid bars recording the level of FST and its decay at different locations across the tunnel empty section. It was

concluded that despite the FST level being far too high with these original screens, its decay was found to be well-behaved: homogenous across the test section and in-line with the previously reported power-law fit decay (Brandt et al. 2004; Fransson et al. 2005). Given the requirement to keep the receptivity linear to facilitate its modelling (Schrader et al. 2010b), a much lower FST was sought. This was achieved with new grids characterised by smaller turbulence-producing elements (i.e. using wires rather than solid bars). A full characterisation of the environment created by the selected turbulence screens is reported in Table 1. Here, the natural level of FST of the facility ($Tu = 0.01\%$) is increased by one order of magnitude to $Tu = 0.33\%$ and $Tu = 0.41\%$ due to the introduction of Grid I and Grid II, respectively. Therefore, while naturally, the tunnel offers a low-turbulence environment (in principle dominated by stationary crossflow instability), the grid-generated cases are classified as high turbulence levels, for which travelling crossflow vortices are expected to govern the instability (Deyhle and Bippes 1996; Radeztsky et al. 1999; Crouch et al. 2015). It must also be considered that acoustic fields also induce velocity irrotational fluctuations that are believed to not influence the crossflow instability (Deyhle and Bippes 1996; Saric et al. 1998b). To isolate the vorticity-induced turbulence, Tu_ω, a filtering procedure based on simultaneous hot-wire data acquisition at different spanwise locations (much greater than the integral length scale of the turbulence) was employed (Nagib et al. 1996). This revealed that a significant amount of the energy contained in the spectrum (when the model is installed in the test section) is highly correlated throughout the tunnel cross section, which would prompt towards its acoustic nature. The Tu due solely due to vortical structures (Tu_ω) is also reported in Table 1. These values are up to 50% lower than the total Tu. To facilitate comparison with previous studies, we adopt Tu_ω as the true measure of the FST in this work, hereafter, following previous work.

Before discussing the effect of an increased FST on flow instability, the conditions downstream of the grids are documented and discussed. Kurian et al. (2011) showed that most turbulence grids show a weak dependence on the location of the measurements (i.e. they introduce in-homogeneity in the turbulence). By acquiring data upstream of the model parallel to its leading edge, the effect of the grids was investigated. These data are presented in Fig. 4. By looking at Fig. 4a, it is clear that the streamwise velocity profiles are fairly flat across the spanwise direction both with and without the grids. The variation in the streamwise velocity fluctuations across the spanwise direction, however, increases incrementally with Tu. This is more clearly visible in Fig. 4b where Grid II appears to introduce some weak heterogeneity in the Tu; its magnitude is, however, fairly small. This is typical of grid-generated turbulence (where the turbulence grids are located downstream of the contraction) as progressively more anisotropy is seen by increasing the FST (Kurian and Fransson 2009). Moreover, Deyhle and Bippes (1996) have shown that mean flow modulation is not an effective means to initiate crossflow vortices; this weak velocity modulation can, therefore, be considered negligible. Finally, the temporal spectra of the velocity fluctuations are shown in Fig. 4c.

Table 1 Details for turbulence grids used in this work

Case ID	d_G	M_{yG}	M_{zG}	Tu	Tu_ω	Λ_x	β	σ	M_{yG}/d_G	M_{zG}/d_G
No grid	–	–	–	0.02	0.01	–	–	–	–	–
Grid I	0.40	11.00	6.50	0.48	0.33	7.90	0.90	0.10	27.50	16.25
Grid II	0.40	11.0	13.00	0.62	0.41	8.60	0.93	0.07	27.50	32.50

Length scales are reported in mm and are measured at the plate's leading edge, Tu is in %

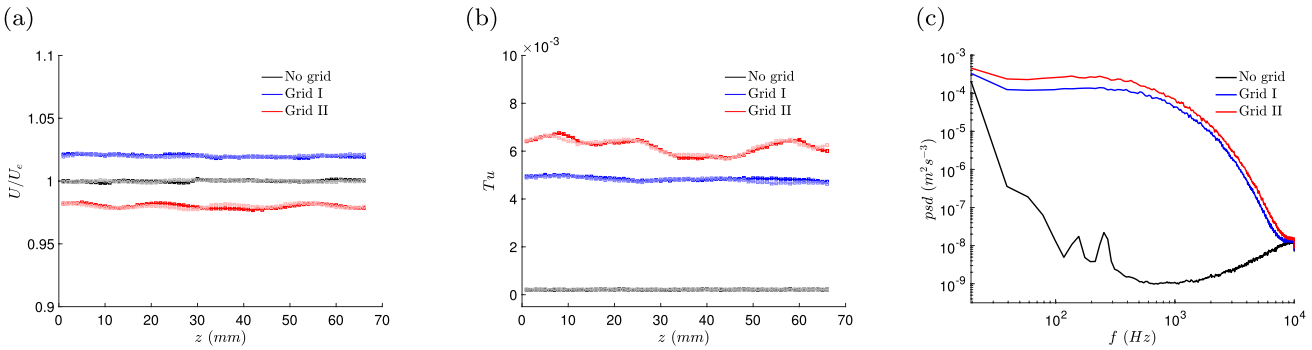

Fig. 4 Spanwise variation in the **a** U/U_e and **b** Tu inside (light) and outside (dark) the boundary layer ($y = 3$ mm and $y = 6$ mm, respectively). **c** Temporal spectra of the fluctuating signals upstream of the model

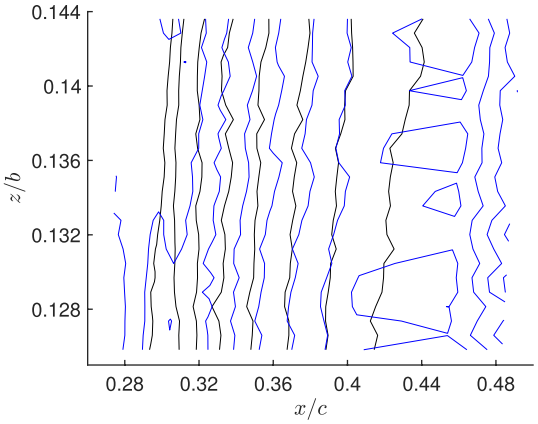

Fig. 5 Contours of U_e/U_∞ within the measurement region for (black) No grid, and (blue) Grid I. Contours levels in range 0.97–1.05 with 0.01 spacing

It is evident how the presence of the screens contributes to a significant broadening of the spectrum across the entire frequency range. This is a typical effect of grid turbulence (e.g. see figure 4 in Downs and White (2013)). In the clean case, two peaks in the spectrum are noticeable at $f = 150$ and 240 Hz. These are associated with the combined effect of the motor driving the tunnel and the presence of the model in the test section, although the lower of the two also corresponds well with frequencies of weak travelling crossflow waves, as further discussed in 3. These are still present—yet negligible—to the transition process in stationary dominated environments (Dagenhart and Saric 1999). See extended discussions on this topic in Placidi et al. (2017) and van Bokhorst (2018).

The streamwise velocity evolution along the measurement domain is presented in Fig. 5. It is shown that the velocity is homogeneous across the spanwise direction and it remains fairly parallel to the leading edge across the measurements domain, signifying that three-dimensional effects are minimal within this region. Furthermore, no statistically significant spanwise periodicity is observed in the mean flow outside the boundary layer. Only two cases are presented for readability purposes, however, the third case follows a similar behaviour.

3 Results and discussion

3.1 Mean flow characterisation and validation

The mean evolution of the boundary layer along the streamwise direction for the reference case is provided in Fig. 6a. Profiles at the first six chordwise locations are presented; these represent stations at which the flow is far ahead of the breakdown to turbulence (see further discussion in Sect.

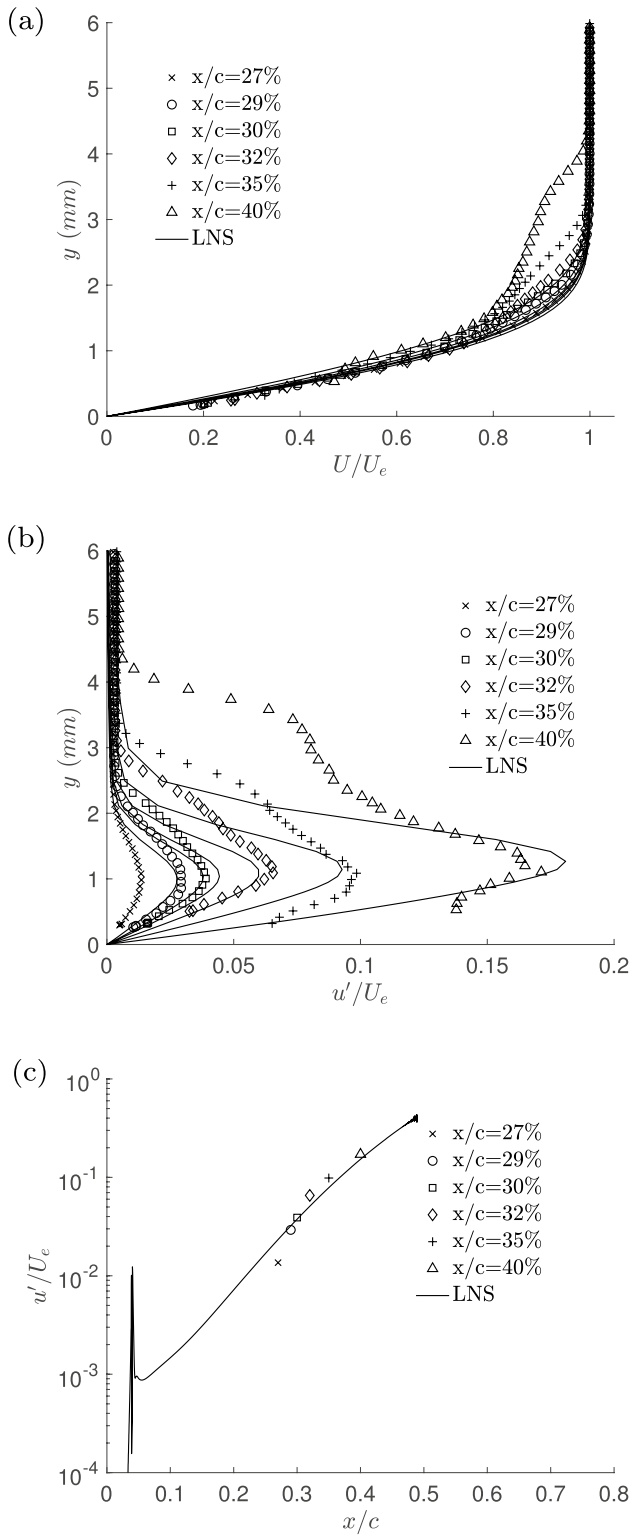

Fig. 6 **a** Mean streamwise velocity profiles and **b** disturbance profiles at several chordwise locations. **c** Disturbance growth over the measured *x*/*c* range. Symbols are the experimental data, solid lines represent the numerical data (LNS)

3.2). The profiles at the first measurement station are typical of a laminar flow regime in the presence of crossflow vortices. A clear change in the profiles' shape and curvature is, however, evident for $x/c = 0.35$ and even more for $x/c = 0.40$. From these stations onward, an inflexion point appears, which is a condition for an inviscid instability. Profiles at the early stage of development show a reasonable concurrence with the numerical predictions (solid black lines), while larger discrepancies appear for large x/c locations; this is perhaps not surprising as the methodology described in Sect. 2.6 was developed to understand the linear stages of the disturbance evolution. It is also important to note that a certain degree of uncertainty affects the identification of the wall location from experimental data acquired with hot-wire sensors. Here, the measured velocity profile was extrapolated downward towards the wall from the first measurement point in a linear fashion, as in Placidi et al. (2020). This procedure is affected by higher uncertainty when the velocity profile is less conventional (e.g. in the presence of infection points for $x/c \geq 0.35$). Measured correspondent velocity fluctuations are reported in Fig. 6b. As expected, the fluctuations reach a maximum inside the boundary layer, while approaching the background FST in the freestream and zero at the wall. This is in-line with the presence of crossflow vortices (Gray 1952; Deyhle and Bippes 1996; Saric and Reed 2003; Serpieri and Kotsonis 2016). The fluctuations reach a magnitude of approximately 20% of the freestream velocity, which is also in-line with previous observation (Malik et al. 1999). Disturbance shape and magnitude are also compared with numerical predictions; considering the experimental uncertainty bounds and the signal-to-noise-ratio for small x/c stations, the agreement is more than satisfactory. Finally, the measured disturbance growth is also compared to the numerical results in Fig. 6c. The growth of the disturbance is well captured, yet the experiments show a slightly earlier onset of exponential growth and an indication on nonlinear behaviour. Overall, the agreement between the measured data and the LNS methodology is satisfactory, despite a slight underestimation of the boundary layer depth by the latter, which is currently under investigation. The findings in Fig. 6 and the good agreement with LSA further discussed in Sect. 3.3 indicate that the data presented agree well with the theory, and builds confidence in the experimental procedure.

3.2 Stationary disturbances

Following the discussion on the characteristics of the incoming flow in the presence of turbulence screens in the previous section, we proceed to evaluate the quantity $rms[(U - \overline{U})/Ue]$, as a proxy of the stationary mode amplitudes (Hunt 2011). These are shown in Fig. 7a–g for different chordwise locations, from $x/c = 27\%$ to $x/c = 45\%$.

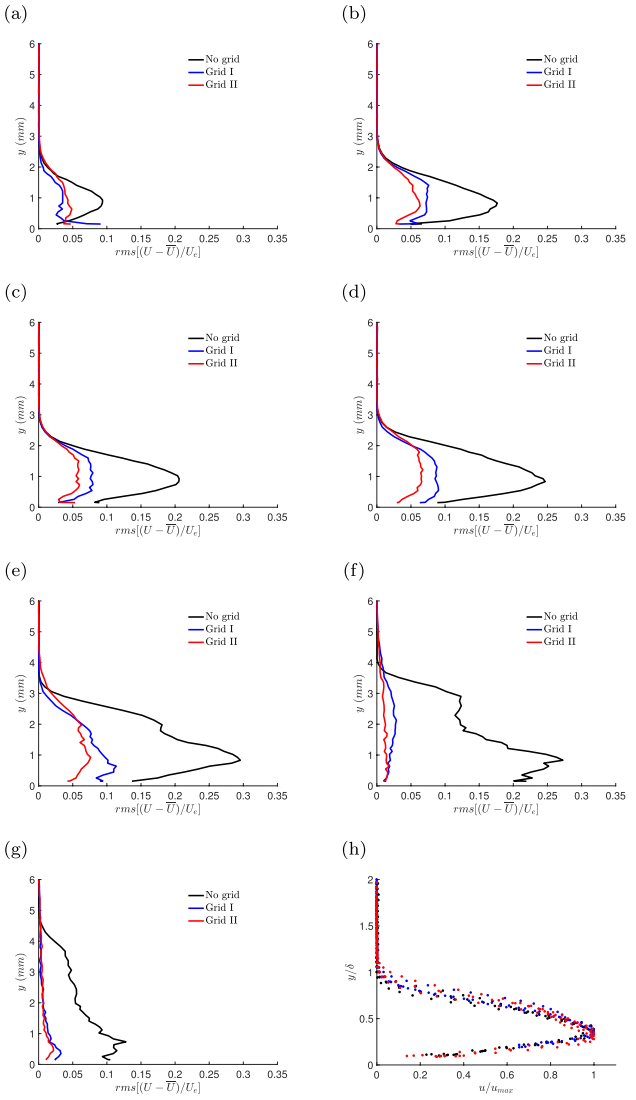

Fig. 7 Amplitude of the primary stationary CF mode at $x/c =$ **a** 27%, **b** 29%, **c** 30%, **d** 32%, **e** 35%, **f** 40%, **g** 45% for the different *Tu*. **h** Universal shape of the disturbance shape within their linear development (i.e. $x/c < 0.35\%$)

At all chordwise locations, the amplitude of the primary stationary modes is shown to be affected by the level of FST. At $x/c = 27\%$ in Fig. 7a, the amplitude of the stationary disturbance is halved by the presence of the grids, and its growth is much hindered compared to the clean low-*Tu* case (compare Fig. 7a–d. While in the low-FST case the stationary mode amplitude magnitude has reached $\text{rms}[(U - \overline{U})/Ue] > 0.25$ at $x/c = 32\%$, this has barely increased in the presence of the screens. Bippes and Lerche (1997) commented that while the initial amplitude of the travelling mode is set by the FST, the initial amplitude of the stationary modes is mostly due to surface roughness. Downs and White (2013) also found the stationary initial amplitude to be independent (within the experimental uncertainty)

of the FST. In the current cases, therefore, this amplitude should not change. It must be stressed, however, that the first measurement location available here is at $x/c = 27\%$ and, therefore, it is not to be considered a 'true' initial disturbance amplitude, given the location of the neutral stability point. It is also important to note that, in the absence of the turbulence screens, the mode shape at $x/c = 35\%$ presents a severe kink, which indicates the onset of the nonlinear phase of the disturbance growth (Reibert 1996; Eppink 2014). This is not so for the cases at higher FST. This behaviour confirms that the higher environmental disturbance level does have an impact on the amplitude and growth of the standing waves, and hence their saturation amplitude (Downs and White 2013). These findings also seem to confirm the previously reported phenomenon in which the stationary disturbances lose their dominant role in the transition process in cases with high *Tu* (Crouch et al. 2015; Radeztsky et al. 1999; Deyhle and Bippes 1996). See the flow breakdown for $x/c = 40\%$ in Fig. 7f despites the low stationary mode amplitude ahead in the previous stations in Fig. 7a–e. This also ties in well with Downs and White (2013) that showed that the stationary modes are largely unaffected by FST only for $Tu < 0.19\%$. Figure 7f and g also suggests that for the cases in the presence of a grid, the flow is already undergoing transition, as the primary mode amplitudes are nearly zero, contrary to the low *Tu* case.

All profiles in Fig. 7a–d at different levels of FST are superimposed and appropriately scaled with the local boundary layer thickness, δ, in Fig. 7h. The concurrence of the data in this figure indicates that the wall-normal disturbance shape can be represented by a universal family of profiles characterised by a single peak at $y/\delta \approx 0.37$, which is in-line with findings in Kurian et al. (2011).

To further explore the stationary crossflow evolution along the chordwise direction, their growth is evaluated, by integrating the area under the local stationary mode amplitude, at all available *x*/*c* locations. This is presented in Fig. 8a. Note that $A_{0,1}$ in this figure represents the amplitude at the first measurement location (i.e. $x/c = 27\%$). It is confirmed that the primary mode growth is much stronger and prolonged in the low-turbulence case compared to the cases in the presence of the grids, where it appears to be significantly hindered. It is also evident from this figure that the saturation amplitude of the stationary modes is dependent on the level of environmental disturbances. This is in-line with indications in Reibert (1996) who discussed how, at low FST, the saturation amplitude of the stationary modes might be higher, and hence greater receptivity to roughness can be expected. It is, however, unclear whether the different initial amplitudes are due to enhanced roughness receptivity or purely to the higher level of environmental disturbances. This, ideally, should be further investigated, however, it is not trivial to decouple these two phenomena. A comparison of the present results with the data in the literature at similar unit Reynolds number and sweep angle is shown in Fig. 8b. Data from Deyhle and Bippes (1996), Reibert (1996), Gladden (2001) are taken from Downs and White (2013). The reader is referred to the latter for further details. The current dataset is also reported in the figure. Black diamonds indicate the measured *Tu* levels, whilst grey symbols represent Tu_ω (i.e. the FST due to vorticity only). The differences in the levels of disturbance saturation at a fixed *Tu* across studies have been previously attributed to differences in (1) the unit Reynolds number across cases ($\mathrm{Re} = 1.1 - 1.7 \times 10^6\ \mathrm{m}^{-1}$), (2) the surface roughness levels, and (3) the experimental facility. The scatter in the data in 8b aids to visualise how sensitive the stationary mode saturation amplitude can be. Note that the current data sit above all previous datasets, meaning that higher saturation amplitudes can be obtained in our facility when compared to previous studies. This is potentially an indication that the development history and the environmental conditions do

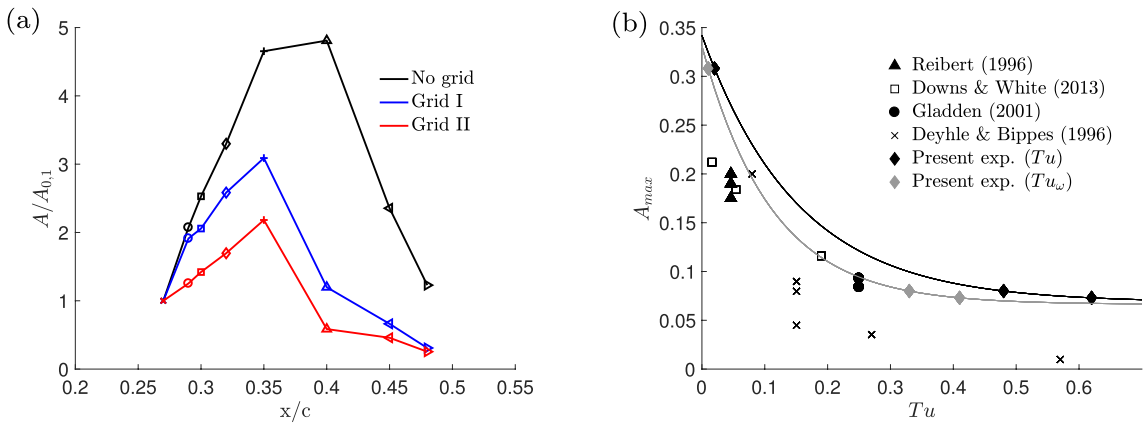

Fig. 8 Growth of primary stationary modes based upon the integral area below the local rms profile ($A_i = 1/\delta_i \int_0^{\delta_i} \mathrm{rms}[(U - \overline{U})/U_e]\,\mathrm{d}y$). Stationary mode saturation amplitude as a function of *Tu* levels from previous and current work

influence the transition process. It must also be stressed that, when considering Tu_ω, the levels of FST (in the clean case) in the current study are the lowest ever reported, which ties in well with the higher saturation amplitude level presented in 8b. Findings like these stress the importance of carrying out transition work in low-turbulence wind tunnels if one wants to model realistic flight scenarios.

3.3 Wavenumber spectra

A simple way to examine the presence and coherency of the primary stationary mode is to calculate the spatial-spectral characteristics of the flow across the spanwise direction. An example of the *psd* of the normalised velocity signals U/U_e at a fixed wall-normal location for all cases is presented in Fig. 9a for $x/c = 0.40$. The normalisation herein employs the total energy across all wavelengths to allow for the magnitude of the spectra to be compared across cases. A distinct peak can be seen in correspondence of the 11.5 mm mode for the low turbulence case, which reflects the critically imposed DREs distribution inferred from LSA. For the higher FST cases, the strength of the primary mode is much reduced confirming findings in Sect. 3.2. The same quantity can be explored focusing solely on the $\lambda = 11.5$ mm wavelength (omitted here), to show a similar trend, where the energy at the critical wavelength for the enhanced FST cases is, again, much lower.

3.4 Unsteady disturbances

Here, we shift our focus to explore the amplitude and growth of unsteady disturbances at the frequencies of interest, intending to isolate the development of the crossflow travelling modes. The bandpass-filtered fluctuations were firstly determined, for each measurement point, by integrating the area under the temporal spectrum within a

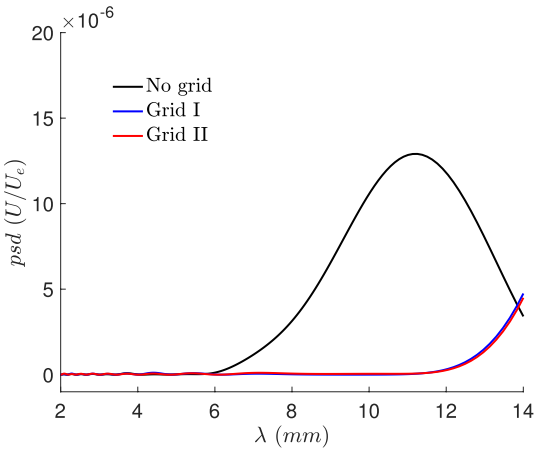

Fig. 9 Spatial *psd* at $x/c = 40\%$ for the three FST levels

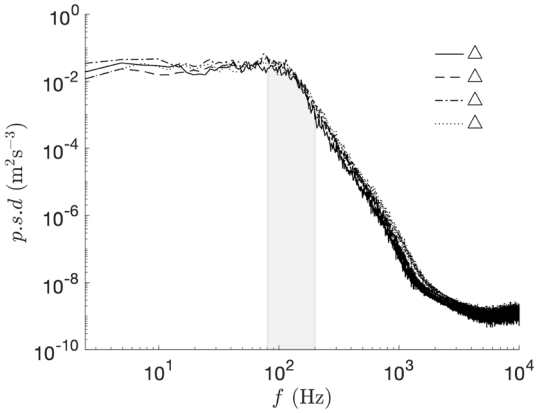

Fig. 10 Examples of typical spectra and bandpass-filtered velocity fluctuations (80 Hz $\leq f \leq$ 200 Hz) at $x/c = 27\%$. The power spectrum density is obtained from a time signal in correspondence with the symbol in Fig. 13e. Case Grid II ($y = 0.80$ mm and four different span locations within a crossflow vortex). The grey area indicates u'_{BF}

certain bandpass range, i.e. between the low-cut-off and the high-cut-off frequencies of interest (f_{LC} and f_{HC}, respectively). Then, the unsteady disturbance field was averaged across the spanwise direction to yield average disturbance profiles, as customarily done in the literature (White and Saric 2005). Figure 10 shows an example of this procedure for the wall-normal location highlighted with the symbol Δ in Fig. 13e, which is later discussed. The area in grey represents the region considered for the integration, so that the $u'_{\mathrm{BP}} = \int_{f_{\mathrm{LC}}}^{f_{\mathrm{HC}}} \text{p.s.d. df}$. The temporal power spectral density is such that verifies Parseval's theorem. Based on LSA, in the measurement region, unsteady waves in the frequency range of 80–200 Hz, are found to be highly amplified. For this reason, we present bandpass-filtered velocity fluctuations within this frequency range next.

Figure 11a–e focuses on the region of growth of the unsteady disturbances ($x/c < 40\%$) as highlighted by its growth in Fig. 11f. To be noted that for the latter calculation, the origin $(u'_{\mathrm{BF}}/U_e, y) = (0, 0)$ was added to the disturbance profiles in Fig. 11a–e.

It is clear from Fig. 11, how the low FST case (black lines) presents a very small magnitude of unsteady disturbances, while these are found to be of much more relevant magnitude for the cases at higher FST. As pointed out in the literature (Downs and White 2013), the amplitude of the unsteady disturbances is much smaller than those of the primary steady modes shown in Fig. 7. This further confirms the findings in Sect. 7 in the fact that steady disturbances dominate the environment for low FST cases (see Fig. 7 and its discussion), while their unsteady counterparts become dominant for higher FST cases—a testimony that the characteristic of the instability has

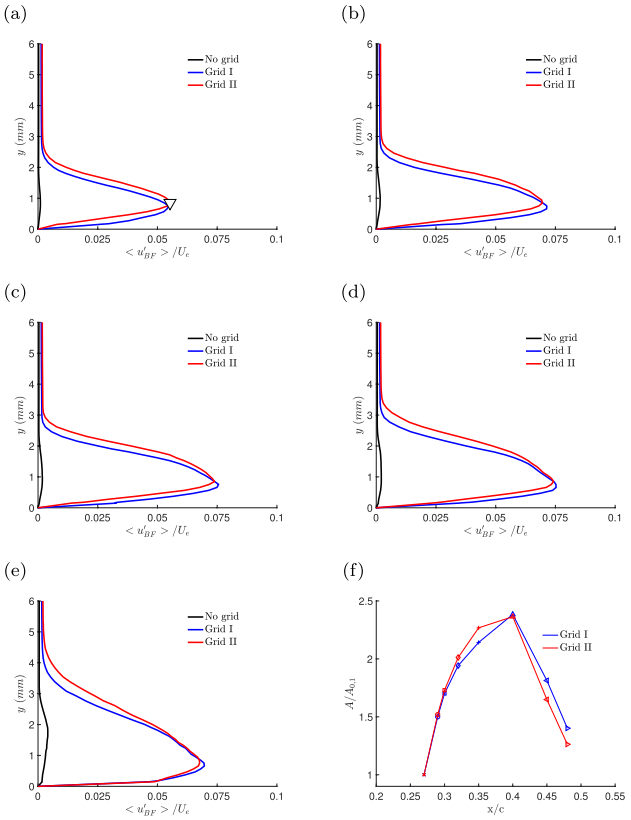

Fig. 11 Unsteady disturbance profiles measured in the CF travelling wave bandpass frequencies (80 Hz $< f <$ 200 Hz) at $x/c =$ **a** 27%, **b** 29%, **c** 30%, **d** 32%, **e** 35%. **f** Growth of unsteady modes based upon the area within the disturbance profile ($A = 1/\delta \int_0^{\delta} u'_{\mathrm{BF}}/U_{\mathrm{e}}] \, \mathrm{d}y$)

changed. It is also interesting to note, that for the measurement stations considered here, the initial amplitude of the unsteady disturbances seems to be largely unaffected by the level of *Tu*, as the maximum amplitudes in Fig 11a are very similar for the Grid I and Grid II cases (see the concurrence of red and blue lines). Figure 11f shows the growth of the unsteady disturbances across the chordwise direction. Here, the case for low FST is omitted due to its very small initial amplitude at the first measurement station which would otherwise skew the results. It is shown that the two turbulence-generating grids produce unsteady disturbances that are largely similar in both amplitude and growth across cases, although some differences appear for $0.3 < x/c < 0.4$. This partly contradicts the findings in Downs and White (2013) who found the rate of growth of the travelling modes to be extremely sensitive to the levels of FST. This may, however, be due to the relatively similar *Tu* levels generated with the two grids employed here, which is much greater than what is customarily considered to be the limit for stationary-modes dominated transition. In this light, the FST levels considered by Downs and White (2013) are much closer to this limit, which could offer another reason for their discrepancies with the work herein.

To further explore the role of the unsteady disturbances in the transition process, we extend our analysis to the whole frequency range; up to frequencies of interest of typical secondary instabilities. These results are shown in Fig. 12. The frequencies of interest were isolated from LSA and previous spectral analysis discussed in Sect. 2.5 and van Bokhorst (2018). Starting from Fig. 12a, this highlights how nearly all of the energy is contained in the very low frequencies ($f < 70$ Hz) in the low FST case when compared to the grid turbulence cases (where the energy at these frequencies is halved and decaying along the chord). If one considers that the limit for $f \to 1$ represents the quasi-stationary modes, this confirms that the stationary modes dominate the problem for low FST. However, these are still present, yet not dominant, for the higher *Tu* cases. Part of energy within this first frequency range of interest is also been previously shown to be related to the blockage caused by the presence of displacement bodies used in the current experimental setup, acoustic noise, and vibrations. This was extensively discussed in van Bokhorst (2018) and Placidi et al. (2020), hence omitted here as these effects are minor and are not considered to drastically influence the transition phenomenon. On the contrary, by looking at the range of interest for the travelling modes previously described in this section, 80 Hz $< f <$ 200 Hz in Fig. 12b, very little energy is found in this range for the low FST case, while the remaining cases show significant amplitudes before the flow starts to break down leading to turbulence for $x/c > 35\%$. Here, the travelling crossflow modes dominate the transition process, as previously discussed. Next, the frequency range 210 Hz$< f <$ 280 Hz is considered in Fig. 12c. This is typical of T–S waves as from evidence from bandpass-filtered fluctuations in this range (omitted here) that show a concentration of energy close to the wall in wall-normal regions correspondent to high mean velocity shear and spanwise locations between CF vortices. The disturbance amplitude in this frequency range is relatively low for all cases and does not show a significant growth; this indicates that the T–S route to transition typical of two-dimensional environments is unlikely relevant in this three-dimensional problem. Finally, Fig. 12d–f presents frequency ranges that have been previously associated with the insurgence of secondary instabilities. Figure 12e shows frequency of interest for Type-I instability (White and Saric 2005); Fig. 12f refers to Type-II instability, which typically occurs at frequencies double those of the Type-I (Wassermann and Kloker 2002). Finally, Fig. 12d refers to low-frequency secondary instability generally associated with the interaction of stationary and travelling modes, also known as Type-III (Janke and Balakumar 2000). These occur typically at frequencies roughly one order of magnitude lower than the previously

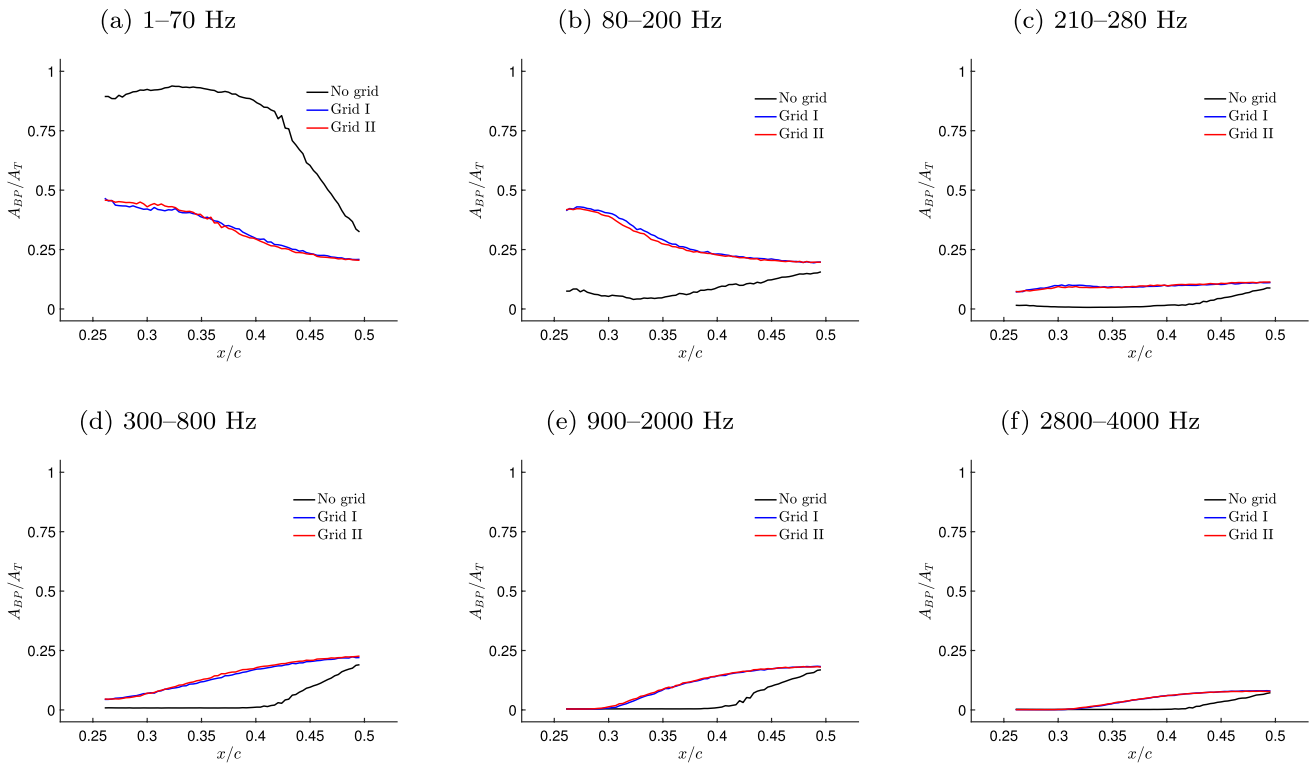

Fig. 12 Bandpass-filtered disturbance amplitude for waves within different frequency ranges. Bandpass-filtered amplitudes are normalised with the overall disturbance amplitude, A_T

discussed Type-II. The reader is referred to Serpieri and Kotsonis (2016) for a further discussion of these instabilities. For all these three secondary instabilities, the cases with higher FST (red and blue lines) show earlier onset of secondary instability compared to the case with lower FST. It was previously discussed how the interaction of the travelling with the stationary modes can be responsible for the migration of energy towards low-frequency instabilities (f = 300–600 Hz). This is very clearly shown in Fig. 12d, where far enough downstream ($x/c \geq 0.3$) the energy relative to this range is increasing for both Grids I and II, while it is still nearly zero for the low-turbulence case. This interaction between travelling and stationary disturbances ties in well with previous observations in the literature (Janke and Balakumar 2000; Bonfigli and Kloker 2007; Serpieri and Kotsonis 2016). Similarly, it can be seen in Fig. 12d how the Type-I instability does not significantly appear for the low FST case before $x/c = 40\%$, which corresponds with the appearance of a highly distorted primary mode shape characterised by a double peak in Fig. 7f. This secondary instability is, however, already present, and growing, in the grid turbulence cases. Likewise, the appearance of the Type-II is much earlier for the high FST cases as shown in Fig. 12f. The earlier onset of secondary instability generally leads to an anticipated transition to turbulence. This is further discussed in Sect. 3.6. It must also be pointed out that the Grid I and Grid II cases perform very similarly in this analysis, where the differences between the energy across cases are largely indistinguishable. This is perhaps due to the same order of magnitude of FST across the two cases. However, this is partly in contrast with previous work that found that the level of *Tu* not only modulates the initial amplitude of the unsteady disturbances but also largely affects their growth rate (Downs and White 2013).

3.5 Characterisation of the secondary instability

To further investigate the characteristics of the instability in each case, colourmaps of the unsteady velocity fluctuations (1 Hz–10 kHz) at appropriate chordwise stations 10% upstream of the transition front (see discussion in Sect. 3.6) are shown in Fig. 13 for all cases. Also shown in the figure are the contours of the normalised mean velocity (black lines), which help to visualise the qualitative shape of the crossflow vortices. Together with the colours, which represent the normalised turbulence fluctuations magnitude, Fourier analysis is used to plot the spectra at the locations indicated by the symbols in Fig. 13a, c, e to highlight what frequency ranges are energised by the instability (see the right column of Fig. 13). The reader is referred to Serpieri and Kotsonis (2016) for an in-depth discussion of the main features distinguishable in these types of plots across the

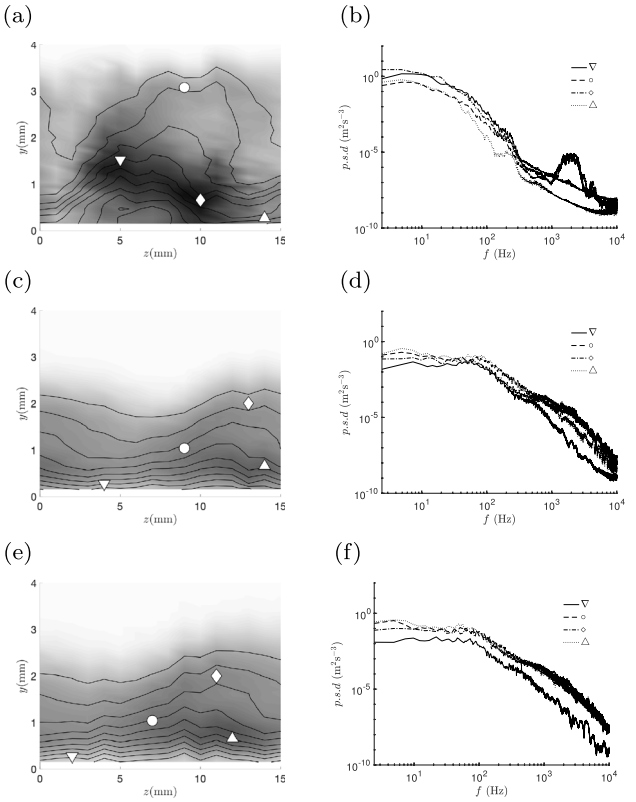

Fig. 13 (Left) Contour lines (black lines) of normalised mean streamwise velocity, U/U_e, superimposed over colourmaps of the streamwise fluctuations, u'/U_e, over one crossflow vortex at **a** $x/c = 0.40$ and **c/e** $x/c = 0.32$. Contours levels every $0.1U_e$, while the colourmap displays $0 < u'/U_e < 0.25$. (Right) Temporal *psd* at the locations of the symbols on the left. No grid, Grid I, and Grid II are presented on the top, centre, and bottom, respectively

chordwise range. Here, we focus predominately on the differences across cases induced by the different FST levels in the late development stages of the instability, where the steady disturbances amplitudes show signs of secondary instability onset (see Fig. 7). For the low turbulence case in Fig. 13a, a strong mean flow modulation is shown corresponding to the forced fundamental wavelength. The mean velocity field is characterised by an inflexion point and unsteady disturbance maxima, also modulated by the fundamental wavelength, which are localised in four distinct areas as highlighted by the symbols; these are further discussed later on in this section. For the two enhanced FST cases in Fig. 13c, e, it is evident how the mean flow contours are much smoother; this is a result of the much weaker primary modes amplitudes (as discussed in Sect. 3.2) and the attenuated mean flow modulation, hence, the less visible large scale organisation of the unsteady fields. Of course, this is also partly due to the upstream chordwise station considered here ($x/c = 32\%$ as opposed to $x/c = 40\%$ for the low FST case); this is, however, justified given the different transition front locations across cases (see Sect. 3.6), and the fact that the higher fluctuation levels within the boundary layer prevent the strong mean flow modulation observed for the low FST cases. Note that although omitted here, contours of mean velocity profiles for $x/c > 32\%$ for the two grid cases, do not show stronger mean flow modulation but instead present evidence of the onset of breakdown to turbulence (see Fig. 7f, g and Sect. 3.6 in support of this statement). The location of the local maxima of the fluctuations for the high FST cases also seems to have changed. These now appear to have been pushed towards the wall; this is not particularly obvious in Fig. 13c, e but it is clearly visible in the high FST cases for $x/c > 35\%$ (omitted here). This is a strong indication that the nature of the instability might have also changed for these cases, as highlighted in previous findings by Downs and White (2013).

To speculate on the nature of the instability, Fourier analysis is also presented for the three cases in Fig. 13. The focus here is on the locations highlighted by the symbols on the left-hand panels of the figure, which correspond to high-fluctuation activity regions. The first of these is located on the outer side of the crossflow vortex and corresponds to its upwelling region where the spanwise velocity gradient is minimum (i.e. Type-I). The second is on the top of the crossflow vortex and it is linked to the wall-normal velocity gradient (i.e. Type-II). Finally, the third area is located on the inside of the vortex, where the spanwise velocity gradient reaches a maximum (i.e. Type-III). Another area of interest is usually the high-momentum region close to the wall within the discrete crossflow vortices; this is also considered in the following Fourier analysis. These areas correspond well to previous findings in the literature. Figure 13b, d, f shows the *psd* (per unit frequency) across the boundary layer for the clean, Grid I and Grid II cases, respectively. These are calculated via the average periodogram with a frequency resolution of 2 Hz.

For the low turbulence case in Fig. 13b, the characteristics of the instability are clearly visible. Here, we can see how most of the energy is contained in the low-frequency band $f < 80$ Hz, however, a weak imprint of the travelling crossflow is still present (80 Hz $< f <$ 200 Hz). At this late development stages, the spectra show clear signs of secondary instability both of Type-I (900 Hz $< f <$ 2000 Hz) and Type-II (2800 Hz $< f <$ 4000 Hz); these are typical of low FST environments (Deyhle and Bippes 1996; Malik et al. 1999; White and Saric 2005; Serpieri and Kotsonis 2016; Downs and White 2013). On the contrary, for the higher FST cases in Fig. 13d, f the energy appears to be enhanced and distributed across a much broader frequency range ($f > 70$ Hz). Of particular note is a much stronger contribution in the frequency range 300-800 Hz is also noticeable for particular locations within the boundary layer. This was absent in the previous case. This Type-III instability has been previously

attributed to the interaction of the strong travelling crossflow vortices (given the high FST) with the stationary waves (Haynes and Reed 2000; Downs and White 2013). These coexisting modes force an unsteady disturbance wave by interaction. Schrader et al. (2009) suggested that, in these cases, it is the combination of the two direct receptivity mechanisms (to roughness and FST), followed by their interaction that triggers unstable waves that eventually lead to turbulence. Finally, for the highest FST cases, despite the earlier chordwise locations of the measurements, the spectra also present the classical broadening across all frequencies typical of the onset of turbulence with high-frequency secondary instability range that is highly excited. The effect of these instabilities on the transition front location is further discussed next.

3.6 Transition onset

Five different x-scans (along the chordwise direction) at different spanwise locations across the experimental model are used to calculate the intermittency factor, γ, as in Fransson et al. (2005), and its variation across the considered spanwise stations, i.e. the dependence of the transition front from the location of the measurements. The curves shown in Fig. 14 with solid lines are averaged across the available five spanwise locations, whilst the symbols represent the variability across each measurement station. The low FST case (in black) shows a much wider spread of the data across the spanwise stations compared to the higher FST cases (in red and blue) that show, on the contrary, an excellent concurrence of the symbols onto the averaged lines. This is an indication of a much flatter (or homogeneous) transition front. White et al. (2001) highlighted how the transition front changes from the classical saw-tooth pattern typical of stationary mode-dominated instability to a flatter front expected for environments dominated by travelling waves. This is because the travelling waves propagate approximately perpendicularly to the local streamline, eroding the sawtooth pattern (Deyhle et al. 1993). Figure 14 is, therefore, a further indication that the transition to turbulence is dominated by stationary modes for low FST but switches to an environment where the unsteady disturbances become dominant for high FST levels, confirming both findings highlighted in the previous sections and previous literature (Downs and White 2013). Furthermore, it can be observed that for the low FST, laminar flow is maintained for the largest chordwise extent; the intermittency factor, in fact, just barely reaches $\gamma = 1$ by the end of the measurement domain. The transition front, however, moves significantly forward in the presence of turbulence grids. In particular, the higher the level of FST, the earlier the transition occurs. The transition front location is arbitrarily identified to be the streamwise position where the spanwise averaged intermittency factor is $\gamma = 0.95$, but this number is per se irrelevant as the findings discussed here are not significantly affected by this choice. With any threshold analysis, as in the case of the intermittency factor, one introduces an element of subjectivity in the results; however, this procedure is well-accepted and is consistently applied to all cases discussed here. Therefore, despite the seemingly arbitrary definition of the transition front location, the trends discussed in the following are found not to depend on this ad hoc parameter. While the transition process occurs at approximately 50% chord in the low-turbulence case, this moves to 44% $\pm$ 0.16% and 43% $\pm$ 0.16% for the Grid I and Grid II cases, respectively. These findings are in-line with previous work confirming that the transition front was found to advance for increased FST levels (Downs and White 2013; Rizzo et al. 2019). It is also interesting to note that the transition front location was also previously found to move to lower critical Reynolds numbers by increasing the FST in Blasius-like boundary layers (e.g. Jonáš et al. 2000; Brandt et al. 2004), although any comparison with 2-D flow requires caution. To conclude, despite the small number of conditions tested herein, where only three cases are considered, an increase in one order of magnitude in FST corresponds roughly to a 10% $\pm$ 0.16% upstream movement of the transition location. It is unclear how this ties in with the work in Hunt (2011), which only observed minor transition effects by a subtle increase in turbulence intensity. A much wider test matrix is required to generate more accurate predictions for the location of the transition front as a function of finer FST adjustments.

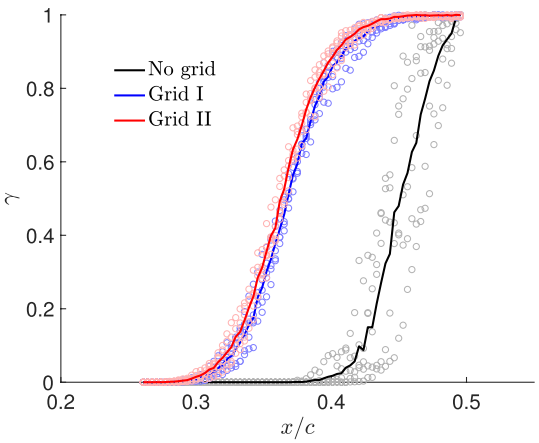

Fig. 14 Intermittency factor, γ, as a function of the chordwise location. $\gamma = 0.95$ is here taken as the transition location

4 Summary and conclusions

Wind tunnel experiments were conducted on the effect of receptivity of crossflow modes to surface roughness and environmental disturbances in the form of freestream

turbulence. The inherent low FST of the facility used here ($Tu < 0.1\%$)—the lowest ever explored experimentally to date—was enhanced by the means of two turbulence grids located upstream of the model. These produced $Tu \approx 0.33\%$ and $Tu \approx 0.41\%$ for a total of three different cases with varying FST levels from low to high, as defined by the previous literature. These are designed to drastically change the transition process from one where the stationary modes are dominant (i.e. low Tu) to cases for which the travelling waves become more significant (i.e. high Tu). For all cases, circular DREs of 24 μm in height were employed close to the neutral stability point to generate fully developed primary disturbances and keep the surface roughness fixed across all cases, in an attempt to decouple the roughness from the FST receptivity. For the same reason, the turbulence grids are designed to generate similar integral length scales of the turbulence.

The results suggest that for $Tu = 0.01\%$ the instability is dominated by stationary modes receptive to critically spaced DREs, as prescribed by LSA. These develop into secondary high-frequency instabilities, which eventually lead to a transition to turbulence via the classical Type-I/Type-II route. Weak travelling modes are still present, but their strength is much lower than the dominant primary modes and they decay quickly as the primary mode strengthens (Dagenhart and Saric 1999). No significant interaction between steady and unsteady disturbances is observed in this case. The findings summarised thus far, confirm most of the available literature on the topic. The saturation amplitude of the steady disturbances, however, deserves a particular note. Here, this is found to be the highest ever recorded in the literature, and it is believed to be connected to the lowest FST characterising the tunnel used in this work. This strongly suggests, as previously hinted by Reibert (1996) but yet unverified due to scarcity of the work at low Tu, that in these conditions the saturation amplitude of the stationary modes might be higher due to the greater receptivity to roughness.

On the contrary, for high FST ($Tu = 0.33\%$ and $Tu = 0.41\%$ herein), strong travelling waves permeate the boundary layer and dominate the stability of these flows at all chordwise stations. The initial amplitude, growth rate, and saturation amplitude of the stationary modes are also affected (i.e. hindered) compared to the case at low FST. These findings vastly confirm previous literature (Downs and White 2013; Crouch et al. 2015), which found that FST affects the development of both the stationary and travelling modes. However, the current data contradicts the earlier work of Bippes and Lerche (1997) who had found the FST to solely influence the initial amplitude of the travelling disturbances. It is also important to point out that the growth rate of the travelling disturbances is found to be largely similar in both grid turbulence cases, which could be seen in contrast with Downs and White (2013) who reported their growth to be highly sensitive to the FST levels. The reader is, however, referred to the discussion on this topic in Sect. 3.4. For these high FST cases, by examining the characteristics of the instability, evidence is offered that is the strong interaction of the travelling and stationary modes that creates waves of different frequencies (300–800 Hz), which have previously been described as Type-III. This interaction produces strongly amplified unsteady disturbances, which are a result of a coupled roughness-turbulence receptivity. This process seems to be absent in the low-turbulence case. For the case at higher FST, the onset of secondary instability appears at a much anticipated chordwise location (i.e. the lower critical Reynolds number).

Finally, the intermittency factor is evaluated for all cases as this encompasses the cumulative receptivity effect of freestream turbulence and surface roughness on cross-flow instability and it allows to correlate the onset of secondary instability to the transition front location. A novel rule of thumb for transition front prediction is proposed: it is found that, for matched roughness conditions, the transition front moves forward by roughly 10% chord when the turbulence intensity increase by one order of magnitude. Further work is, however, necessary to enrich the Tu test matrix to be able to more accurately correlate changes in the FST with the movement of the transition front location with the aim of transition prediction modelling.

Acknowledgements The authors would like to acknowledge the financial support of the EPSRC under grant ref. EP/L024888/1 UK NWTF coordinated by Imperial College, and Innovate UK under grant ref. 113022 ALFET, coordinated by Airbus. We are also indebted to Prof. Michael Gaster for his guidance, support, and fruitful discussions on this topic and to Dr Evelien van Bokhorst for providing the LSA data.

Author contributions The experimental design was carried out by Dr. MP and Professor CJA. Experimental data collection and analysis were performed by Dr. MP, who also wrote the first draft of the manuscript. Numerical experiments were designed and run by Dr. RA. All authors have commented/contributed to each version of this manuscript. Prof. CJA and Dr. SR coordinated activities within the funding programme.

Declarations

Conflict of interest The authors declare that they have no conflict of interest or competing interests.

Ethical approval Not applicable.

Open Access This article is licensed under a Creative Commons Attribution 4.0 International License, which permits use, sharing, adaptation, distribution and reproduction in any medium or format, as long as you give appropriate credit to the original author(s) and the source, provide a link to the Creative Commons licence, and indicate if changes were made. The images or other third party material in this article are included in the article's Creative Commons licence, unless indicated otherwise in a credit line to the material. If material is not included in

the article's Creative Commons licence and your intended use is not permitted by statutory regulation or exceeds the permitted use, you will need to obtain permission directly from the copyright holder. To view a copy of this licence, visit http://creativecommons.org/licenses/by/4.0/.

References

Atkin CJ (2004) Calculation of laminar boundary layers on swept-tapered wings. Technical Report Report FST/TR025107. QinetiQ Ltd

Atkin CJ, Poll DIA (1996) Correlation between linear stability analysis and crossflow transition near an attachment line. North-Holland, Amsterdam

Baranov SA, Chernyshev SL, Khomich VY, Kiselev AP, Kuryachii AP, Moshkunov SI, Rebrov IE, Sboev DS, Tolkachev SN, Yamshchikov VA (2021) Experimental cross-flow control in a 3D boundary layer by multi-discharge plasma actuators. Aerosp Sci Technol 112:106643

Bertolotti FP (2000) Receptivity of three-dimensional boundary-layers to localized wall roughness and suction. Phys Fluids 12(7):1799–1809. https://doi.org/10.1063/1.870428

Bippes H, Lerche, T (1997) Transition prediction in three-dimensional boundary-layer flows unstable to crossflow instability. . In: AIAA—28th fluid dynamics conference, Snowmass Village, CO, USA. AIAA, pp 97–1906

Bonfigli G, Kloker M (2007) Secondary instability of crossflow vortices: validation of the stability theory by direct numerical simulation. J Fluid Mech 583:229

Borodulin VI, Ivanov AV, Kachanov YS, Mischenko DA, Örlü R, Hanifi A, Hein S (2018) Quantitative study of localized mechanisms of excitation of cross-flow instability modes in a swept-wing boundary layer. J Phys Conf Ser 1129:012008

Borodulin VI, Ivanov AV, Kachanov YS, Mischenko DA, Örlü R, Hanifi A, Hein S (2019) Experimental and theoretical study of swept-wing boundary-layer instabilities. Unsteady crossflow instability. Phys Fluids 31(6):064101

Borodulin VI, Ivanov AV, Kachanov YS, Roschektaev AP (2013) Receptivity coefficients at excitation of cross-flow waves by free-stream vortices in the presence of surface roughness. J Fluid Mech 716:487–527

Brandt L, Schlatter P, Henningson DS (2004) Transition in boundary layers subject to free-stream turbulence. J Fluid Mech 517:167–198

Bruun HH (1995) Hot-wire anemometry principles and signal analysis. Oxford University Press. ISBN-10: 0198563426

Butler A, Wu X (2018) Stationary crossflow vortices near the leading edge of three-dimensional boundary layers: the role of non-parallelism and excitation by surface roughness. J Fluid Mech 845:93–140

Carpenter A, Saric W, Reed H (2009) In-flight receptivity experiments on a 30-degree swept-wing using micron-sized discrete roughness elements. In: 47th AIAA aerospace sciences meeting including the new horizons forum and aerospace exposition 5–8 January 2009, Orlando, Florida, pp AIAA 2009–590

Carpenter Mark H, Cholemari Murali R, Craik A DD, Chang Chau-Lyan, Li F (2010) Excitation of crossflow instabilities in a swept wing boundary layer. In: 48th AIAA aerospace sciences meeting Orlando, Florida, pp AIAA 2010–378

Carrillo RB, Reibert MS, Saric WS (1996) Distributed roughness effects on stability and transition in swept wing boundary layers. Technical Report NASA-CR-203580. NASA-Langley Research Center

Chernyshev SL, Ivanov AI, Kiselev AP, Kuzminsky VA, Sboev DS, Zhigulev Sergey V (2011) Investigations of influence of free stream turbulence and acoustic disturbances on the laminar-turbulent transition on lv6 airfoil and swept wing models. In: 49th AIAA aerospace sciences meeting including the new horizons forum and aerospace exposition. AIAA, pp AIAA 2011–210

Crouch JD, Ng LL, Kachanov YS, Borodulin VI, Ivanov AV (2015) Influence of surface roughness and free-stream turbulence on crossflow-instability transition. Procedia IUTAM 14:295–302

Dagenhart JR, Saric WS (1999) Crossflow stability and transition experiments in swept-wing flow. NASA/TP-1999-209344

Deyhle H, Bippes H (1996) Disturbance growth in an unstable three-dimensional boundary layer and its dependence on environmental conditions. J Fluid Mech 316:73–113

Deyhle H, Hoehler G, Bippes H (1993) Experimental investigation of instability wave propagation in a three-dimensional boundary-layer flow. AIAA J 31(4):637–645. https://doi.org/10.2514/3.11597

de Paula IB, Würz W, Mendonça MT, Medeiros MAF (2017) Interaction of instability waves and a three-dimensional roughness element in a boundary layer. J Fluid Mech 824:624–660

Downs RS (2012) Environmental influences on crossflow instability. PhD thesis

Downs RS, White EB (2013) Free-stream turbulence and the development of cross-flow disturbances. J Fluid Mech 735:347–380

Eppink J (2014) The interaction of crossflow instabilities and a backward facing step in swept boundary layer transition. PhD thesis

Fransson JHM, Matsubara M, Alfredsson HP (2005) Transition induced by free-stream turbulence. J Fluid Mech 527:1–25

Fransson JHM, Shahinfar S (2020) On the effect of free-stream turbulence on boundary-layer transition. J Fluid Mech 899:A23

Gladden RD (2001) Crossflow transition in elevated free stream turbulence. PhD thesis

Gray W (1952) The effect of wing sweep on laminar flow. Technical Report RAE TM Aero. 255. Royal Aircraft Establishment

Groot KJ, Serpieri J, Pinna F, Kotsonis M (2018) Secondary crossflow instability through global analysis of measured base flows. J Fluid Mech 846:605–653

Guissart A, Romblad J, Nemitz T, Tropea C (2021) Small-scale atmospheric turbulence and its impact on laminar-to-turbulent transition. AIAA J 1–11

Haynes TS, Reed HL (2000) Simulation of swept-wing vortices using nonlinear parabolized stability equations. J Fluid Mech 405:325–349

Hunt LE (2011) Boundary-layer receptivity to three-dimensional roughness arrays on a swept-wing. PhD thesis

Hutchins N, Nickels TB, Marusic I, Chong MS (2009) Hot-wire spatial resolution issues in wall-bounded turbulence. J Fluid Mech 635:103–136

Janke E, Balakumar P (2000) On the Secondary Instability of Three-Dimensional Boundary Layers. Theor Comput Fluid Dyn 14:167–194

Jonáš P, Mazur O, Uruba V (2000) On the receptivity of the by-pass transition to the length scale of the outer stream turbulence. Eur J Mech B Fluids 19(5):707–722

Katasonov MM, Sadovskiy IA (2021) Experimental investigation of disturbances generated by impulse deflection of the membrane in the swept wing boundary layer under the moderate free—Stream turbulence level. In: AIP conference proceedings, vol 2351. AIP Publishing, pp 040021–1-040021–6

Kurian T, Fransson JHM (2009) Grid-generated turbulence revisited. Fluid Dyn Res 41(2):021403

Kurian T, Fransson JHM, Alfredsson HP (2011) Boundary layer receptivity to free-stream turbulence and surface roughness over a swept flat plate. Phys Fluids 23(3):034107

Malik MR, Li JD, Choudhari MM, Chang C-L (1999) Secondary instability of crossflow vortices and swept-wing boundary-layer transition. J Fluid Mech 399:85–115

Morkovin MV (1969) On the many faces of transition. In: Viscous drag reduction. Viscous Drag Reduction, pp 1–31
Mughal M (2006) Stability analysis of complex wing geometries: parabolised stability equations in generalised non-orthogonal coordinates. In: 36th AIAA fluid dynamics conference and exhibit
Mughal SM, Ashworth Richard M (2013) Uncertainty quantification based receptivity modelling of crossflow instabilities induced by distributed surface roughness in swept wing boundary layers. In: AIAA 2013–3106 43rd AIAA fluid dynamics conference, 24–27 June, San Diego, CA
Nagib HM, Gravante SP, Wark CE (1996) Extraction of turbulent wall-pressure time-series using an optimal filtering scheme. Exp Fluids 22:14–22
Nitschke-Kowsky P, Bippes H (1988) Instability and transition of a three-dimensional boundary layer on a swept flat plate. Phys Fluids 31(4):786–795
Placidi M, Gaster M, Atkin CJ (2020) Acoustic excitation of Tollmien–Schlichting waves due to localised surface roughness. J Fluid Mech 895(2262):13
Placidi M, van Bokhorst E, Atkin CJ (2017) Advanced laminar flow enabling technologies (ALFET) Technical Report. City University of London, Technical Report
Radeztsky RH Jr, Reibert MS, Saric WS (1999) Effect of isolated micron-sized roughness on transition in swept-wing flows. AIAA J 37(11):1370–1377
Reed HL, Saric WS (1989) Stability of three–dimensional boundary layers. Annu Rev Fluid Mech 21:235–284
Reibert MS (1996) Nonlinear stability saturation and transition in crossflow dominated boundary layers. PhD thesis
Rizzo P, Serpieri J, Kotsonis M (2019) Sensitivity of crossflow transition to free-stream conditions and surface roughness. In: AIAA SciTech forum. https://doi.org/10.2514/6.2019-11337-11 January 2019, San Diego, California AIAA Scitech 2019 Forum. AIAA, p 1133
Saric WS (2008) Flight experiments on local and global effects of surface roughness on 2-D and 3-D boundary-layer stability and transition. Technical Report AFRL-SR-AR-TR-08-0468. Texas A &M University
Saric WS, Carpenter AL, Reed HL (2011) Passive control of transition in three-dimensional boundary layers, with emphasis on discrete roughness elements. Philos Trans R Soc A Math Phys Eng Sci 369(1940):1352–1364. https://doi.org/10.1098/rsta.2010.0368
Saric WS, Carrillo RB, Reibert MS (1998) Leading-edge roughness as a transition control mechanism. In: AIAA98 36th aerospace sciences meeting and exhibit. AIAA98 36th Aerospace Sciences Meeting and Exhibit January 12–15, 1998 Reno, NV, pp AIAA 98–0781
Saric WS, Carrillo RB, Reibert MS (1998) Nonlinear stability and transition in 3-D boundary layers. Meccanica 33(5):469–487
Saric WS, Reed HL (2003) Crossflow instabilities–theory & technology. In: AIAA 2003-0771, pp 1–9
Saric WS, Reed HL, Kerschen EJ (2002) Boundary-layer receptivity to freestream disturbances. Annu Rev Fluid Mech 34:291–319
Saric WS, Reed HL, White EB (2003) Stability and transition of three-dimensional boundary layers. Annu Rev Fluid Mech 35(1):413–440
Schrader L-U, Amin S, Brandt L (2010) a Transition to turbulence in the boundary layer over a smooth and rough swept plate exposed to free-stream turbulence. J Fluid Mech 646:297
Schrader L-U, Brandt L, Henningson DS (2009) Receptivity mechanisms in three-dimensional boundary-layer flows. J Fluid Mech 618:209
Schrader L-U, Tempelmann D, Brandt L, Hanifi A, Henningson DS (2010b) Numerical study of boundary-layer receptivity on a swept wing. Technical Report, Royal Institute of Technology
Serpieri J, Kotsonis M (2016) Three-dimensional organisation of primary and secondary crossflow instability. J Fluid Mech 799:200–245
Serpieri J, Kotsonis M (2018) Conditioning of unsteady cross-flow instability modes using dielectric barrier discharge plasma actuators. Exp Thermal Fluid Sci 93:305–318
Sharma PK, Sengupta TK (2019) Effect of frequency and wavenumber on the three-dimensional routes of transition by wall excitation. Phys Fluids 31(6):064107
Takagi S, Itoh N (1994) Observation of traveling waves in the three-dimensional boundary layer along a yawed cylinder. Fluid Dyn Res 14(4):167–189
van Bokhorst E (2018) Forcing of the primary and secondary crossflow instability. PhD thesis
van Bokhorst E, Atkin CJ (2017) Wall forcing of the secondary crossflow instability. In: 47th AIAA fluid dynamics conference, 5–9 June 2017 Denver, Colorado, 47th AIAA fluid dynamics conference, vol. 316. 47th AIAA Fluid Dynamics Conference, pp AIAA 2017–3458
Wassermann P, Kloker M (2002) Mechanisms and passive control of crossflow-vortex-induced transition in a three-dimensional boundary layer. J Fluid Mech 456:49–84
Westin JKA, Boiko AV, Klingmann BGB, Kozlov VV, Alfredsson HP (1994) Experiments in a boundary layer subjected to free stream turbulence. Part 1. Boundary layer structure and receptivity. J Fluid Mech 281:193–218
White EB, Saric WS (2005) Secondary instability of crossflow vortices. J Fluid Mech 525:275–308
White EB, Saric WS, Gladden RD, Gabet PM (2001) Stages of swept-wing transition. In: AIAA 2001 39th aerospace sciences meeting & exhibit. AIAA 2001 39th aerospace sciences meeting & exhibit, 8–11 January 2001, Reno, Nevada, pp AIAA 2001–0271
Yadala S, Hehner MT, Serpieri J, Benard N, Dörr PC, Kloker MJ, Kotsonis M (2018) Experimental control of swept-wing transition through base-flow modification by plasma actuators. J Fluid Mech 844:R2

Publisher's Note Springer Nature remains neutral with regard to jurisdictional claims in published maps and institutional affiliations.